Supporting Information

Single-Particle Spectroscopy Reveals Heterogeneity in Electrochemical Tuning of the Localized Surface Plasmon

Chad P. Byers[†], Benjamin S. Hoener[†], Wei-Shun Chang[†], Mustafa Yorulmaz[†], Stephan Link[†,#,*], Christy F. Landes[†,#,*]

[†] Dept. of Chemistry, Rice Quantum Institute, Laboratory for Nanophotonics; [#] Dept. of Electrical and Computer Engineering, Rice University, Houston, Texas 77005, United States

[*] Corresponding authors, emails: slink@rice.edu, cflandes@rice.edu

SI information: 24 pages, 9 figures, 1 table

SI Table of Contents

1. Methods

1.1 Spectroelectrochemical cell preparation

An optically transparent electrochemical cell was fabricated for use in transmission dark field geometry. A hybrid working electrode was constructed by depositing 50 nm gold nanoparticles onto clean ITO (Thermo Scientific). The ITO coverslip along with an uncoated glass coverslip were cleaned by soaking in a 10% NaOH aqueous solution at 55° C for 30 minutes. The slides were then rinsed in deionized water, washed twofold in an ultrasonic bath of deionized water for 10 minutes, and finally rinsed extensively in Millipore filtered deionized water. The slides remain in an ultrasonic bath until being removed and dried quickly with a directed dry N_2 jet.

50 nm gold nanoparticles were drop cast from water onto the ITO surface dried with a dry nitrogen jet. To remove excess gold nanoparticles and surfactant, a threefold rinsing step was performed with 200 µl of Millipore-filtered deionized water micropipetted onto the ITO surface. The large water drop was held on the slide surface for 30 seconds and then removed. The ITO coated slide with adsorbed gold nanoparticles was then plasma cleaned in an O_2 plasma at 200 mTorr for 40 seconds to destroy remaining surfactant.

The transparent electrochemical cell was built stepwise in a custom aluminum sample holder. Copper magnet wire was soldered to short electrode leads that form the various electrodes: silver wires (Sigma Aldrich) for auxiliary electrode, quasi-reference electrode, and as an intermediate lead to the ITO/gold colloid hybrid working electrode.

Two doubly adhesive silicone spacers (25×25×0.12 mm ID: 13 mm) and one nonadhesive silicone spacer (25×25×0.5 mm ID: 15 mm) (Grace BioLabs) were stacked atop the

ITO/gold nanoparticle working electrode. A silver wire lead to the working electrode made ohmic contact with the ITO surface via physical connection and a secondary layer of silver paint (SPI Supplies). The reference electrode was located < 0.12 mm from the working electrode but was not in contact with the working electrode surface. The auxiliary electrode was electrically isolated from the reference and working electrodes as well as their leads and was coiled into a radially symmetric pattern around the circumference of the cell. The cell was overfilled with electrolyte, the top coverslip was placed, and excess electrolyte was removed prior to sealing the cell. A top plate sealed the cell mechanically and remained assembled. Before each experiment, the cell's open circuit potential was measured and the cell underwent 50 voltammetric cycles in the cathodic range prior to spectroelectrochemical measurements. Routine cyclic voltammetry measurements were performed to ensure uniformity between cells.

1.2 Single spectrum processing and analysis

Several optical and electronic effects justified the correction of scattering spectra. Because the Tungsten-Halogen excitation lamp had a non-flat spectral output through the visible range, the measured scattering spectrum of a nanoparticle was a linear convolution of the scattering spectrum, the spectrum of the illumination source, and the instrument response. Spectra were corrected for local background due to diffuse light scattered from out-of-focus areas of the sample or from the substrate, and for the non-flat lamp spectrum according to:

$$Particle\ Scattering\ Spectrum = \frac{scattering\ spectrum - background\ spectrum}{lamp\ spectrum - dark\ counts}$$

Following the spectral processing, a single Lorentzian curve was fit using a non-linear least squares fitting algorithm implemented in Matlab. All spectral fitting was performed on an energy scale.

1.3 Single nanoparticle spectroelectrochemical tuning measurements

To investigate electrochemical tuning of plasmonic nanoparticles during cyclic voltammetry on the second time scale, single nanoparticles were observed by positioning the spectrometer slit at the center of a particular nanoparticle in the image with a 100 μm slit width, corresponding to a square integration area of 2.52 μm^2 (1.59 μm side length). The vertical dimension of this area was achieved programmatically by selecting and binning the corresponding CCD pixels rows.

The electrochemical workstation was controlled through Labview automation software. In order to preserve the internal timing of both the potentiostat and the Labview spectral acquisition program, a transistor-transistor-logic (TTL) pulse was generated using a data acquisition card (National Instruments) to trigger the internal function generator of the electrochemical workstation. Figure S1 shows a diagrammatic representation of the dark field hyperspectral microscope with full electrochemical integration.

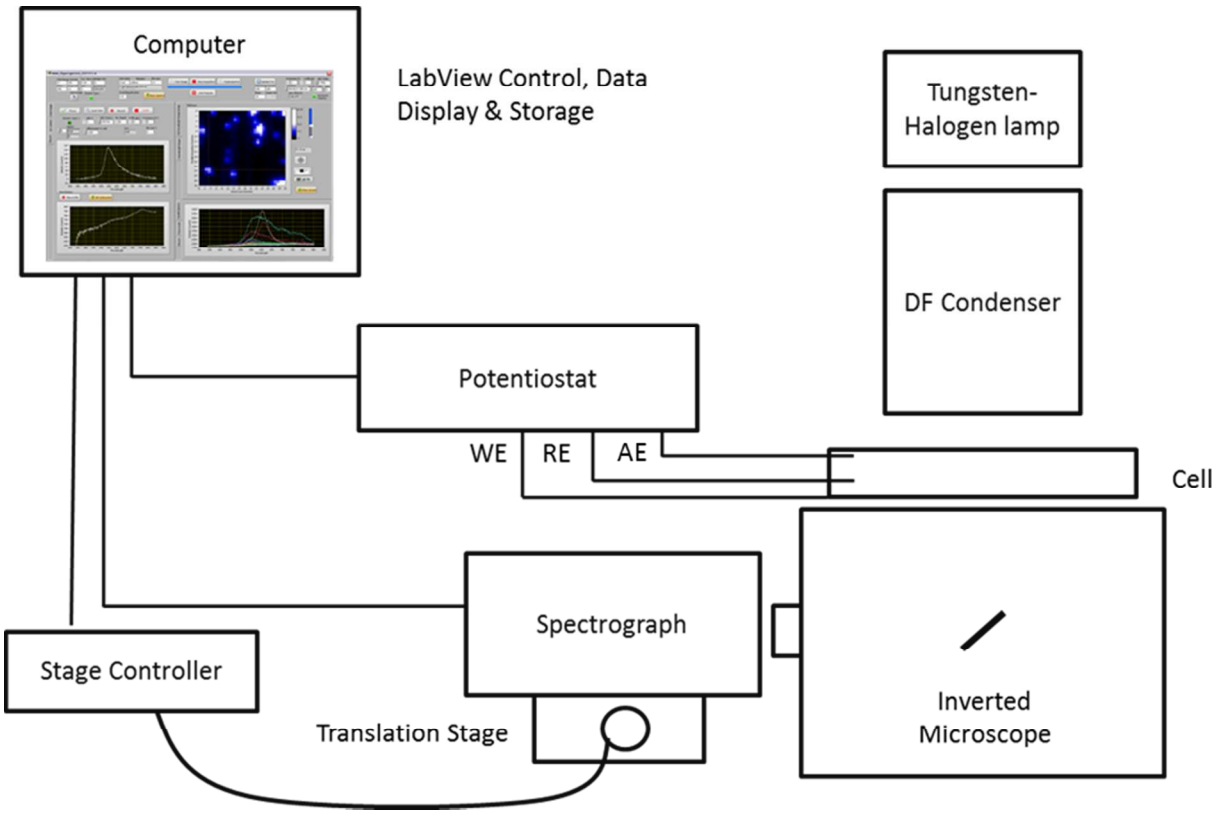

Figure S1. Instrument setup diagram for the spectroelectrochemical hyperspectral dark field microscope. WE: working electrode, RE: reference electrode, AE: auxiliary electrode.

1.4 Hyperspectral implementation and analysis

The dark field hyperspectral microscope was composed of three main hardware components: an inverted dark field microscope, an imaging spectrograph, and a linear translations stage. The role of the translation stage was to programmatically move the entrance slit of the imaging spectrograph through the image of the sample produced by the microscope. This configuration is known as a pushbroom imaging scheme as the sensor array (an imaging spectrograph in this case) sweeps along the image plane and builds a data cube serially.[1]

Nanoparticles in the electrochemical cell were excited with white light under a transmission dark field geometry. Scattered light was collected by an oil immersion objective and could be directed to the eyepiece for visual inspection or for image capture with a mounted digital SLR camera (Canon). Scattered light could also be directed to one of two side ports. At the left side port, there was the imaging spectrometer setup. The CCD camera had 400 rows and 1340 columns of 20×20 μm pixels. The imaging spectrograph was also equipped with an adjustable bilateral entrance slit with minimum width of 10 μm and two electronically addressable and controllable diffraction gratings. The grating used for all measurements in this work was a 300 lines/mm echellette grating that is efficiency optimized for first order refraction at 500 nm (blaze angle: 4.30º).

To move the entrance slit through the image plane at the microscope side port, the entire spectrograph was mounted onto a stack of two orthogonal linear translation stages. The stage with axis of motion perpendicular to the image plane was fitted with a manual micrometer, and was used to position the spectrograph entrance slit in the image plane. The second linear translation stage with translation axis parallel to the image plane was outfitted with a programmatically controlled linear actuator. The actuator had a travel speed of 1 mm/s and a minimum step size and precision of 50 nm. The step size used in hyperspectral imaging was 20 μm. This corresponded to a position uncertainty on the order of 0.25% and an actual travel time of 20 ms. Given that the acquisition time per exposure in hyperspectral image acquisition was rarely less than 500 ms, the scan speed and position precision of this stage were more than adequate.

Finally, in order to align the entrance port of the spectrograph with the left side exit port of the microscope, the entire microscope was raised with custom solid aluminum legs. Due to the

Cartesian nature of this setup, alignment of the spectrometer entrance slit travel plane and the image plane at the microscope side port was of paramount importance. Once alignment was achieved, all components are hard mounted to an active vibration isolated optical table.

In hyperspectral imaging, it is useful to refer to the 3-dimensional data set as a data cube. Two dimensions of the cube consist of spatial information. For simplicity, we will call these dimensions x and y. The third dimension is light energy. We will call this the c dimension, short for color. Therefore, each plane (x-y) normal to the energy (c) dimension is simply a spatial map of the light intensity for a specific energy window. In a push broom collection scheme, spectra are collected in parallel along the extent of the sensor. For each exposure, one y-c plane of the data cube is populated. The sensor is then moved in the x direction, and takes another exposure. In this manner, the data cube is populated in parallel in the y dimension and in serial in the x dimension. Practically, this adds time dependence to the acquired data. Because each x-c plane of data is acquired in separate exposures, the hyperspectral image records data over a time period roughly equal to the number of exposures multiplied by the sum of the exposure time and the stage movement time. Other small time constants also contribute to the total acquisition time including control software delays, CCD camera readout time, and data transfer time.

In the current setup, many of these processes were parallelized in order to minimize the impact of compounding time delays. For instance, following an exposure, the register of a CCD camera must clear each column of pixels and convert these to a readable binary signal in serial. The readout time for the CCD camera is therefore dependent on the amount of data that it must read at each exposure. For large images, the CCD camera clearing time can be of the order of the stage movement time (tens of milliseconds). By parallelizing stage movement with CCD camera

clearing, data transfer, and storage, the major time components were reduced to stage movement time and exposure time.

For each exposure, ~ 50 to 300 spectra were recorded. We designed the software interface to provide the operator with useful information about the incoming data in real-time and also to allow quick post-acquisition processing. This gave the user access to data metrics such as signal-to-noise (SNR) and signal-to-background ratios (SBR), background corrected spectra, and data cube sectioning to make on the fly adjustments to any of the instrument's many parameters. For instance, in order to increase the SNR, the user could make an informed decision of whether to increase the exposure time, decrease the CCD camera clearing rate to reduce shot noise, or decrease the wavelength or spatial resolution. These parameters were adjustable, allowing a user to maximize data quality while minimizing data acquisition time.

1.5 Reconstructed true-color RGB images from hyperspectral data

Hyperspectral imaging allowed us to collect large amounts of spectral information in little time. One data analysis technique involved identifying nanoparticles and extracting single nanoparticle scattering spectra from the hyperspectral data cube, as discussed in Section 1.2 and 1.3. This analysis scheme broke down the data set into small usable pieces. In order to get a general overview of the entire hyperspectral image, another analysis technique was needed to condense the data into a visible image representation. For this purpose, we aimed to create a color image from the hyperspectral data cube.

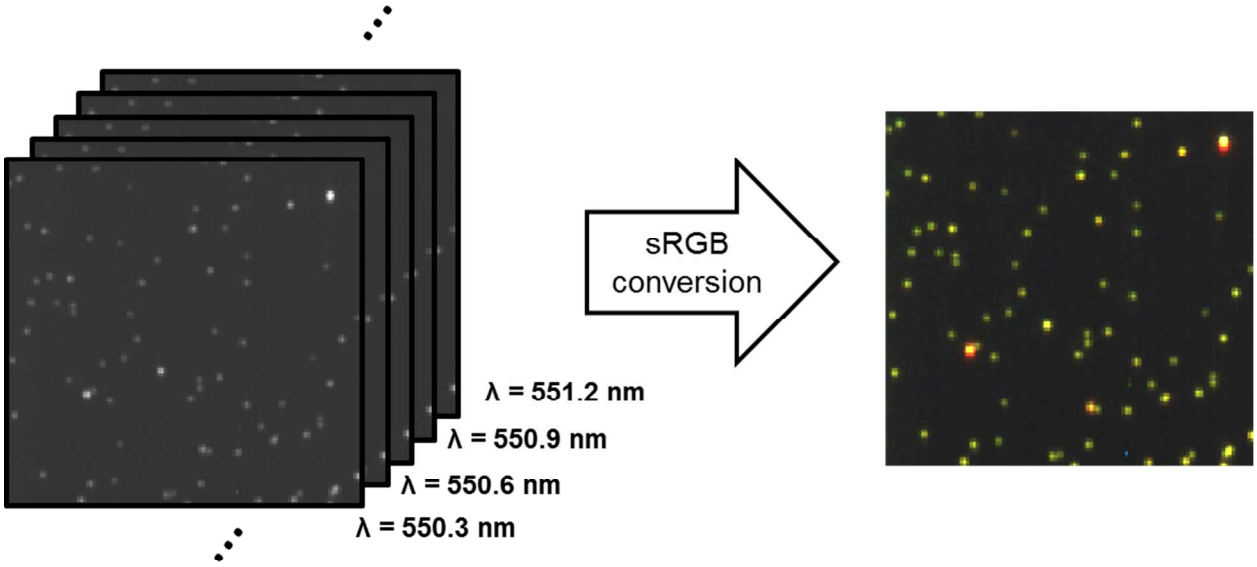

Figure S2. Basic motivation and principle of converting a collection of monochrome images (hyperspectral data cube) to a single three-layer RGB image. The image shown is a 50×50 pixel image (32×32 μm) of 50 nm gold nanoparticles in the electrochemical cell described in Section 1.1.

We chose to represent our data in the sRGB data format because data was nearly always viewed on computer screens and projectors and this colormap was optimized for these media. To convert a resolved spectrum to its constituent red, green, and blue components, we multiplied a spectral response function for the sRGB colorspace to each constituent spectrum of the hypespectral image. We then summed the red, green, and blue components separately to compile the three layer RGB image. By using the background and flatfield corrected spectra in this calculation, we captured the true color of scatterers as they would appear under flat white illumination.

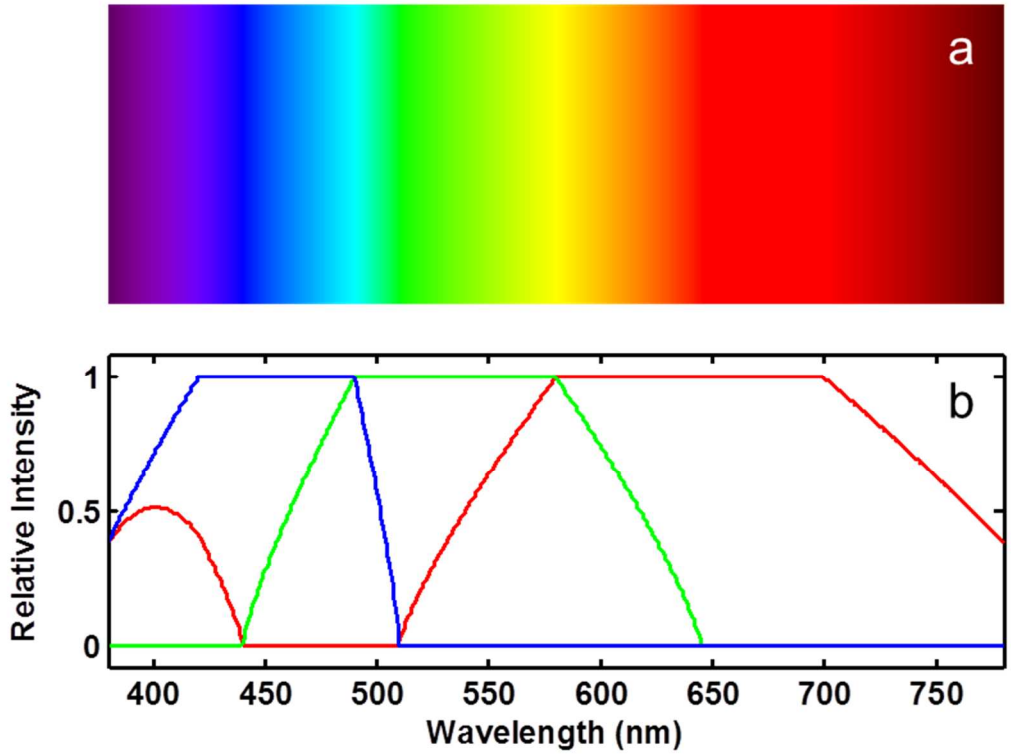

Figure S3. Spectral response function used to construct RGB images from hyperspectral images. (a) The familiar RGB image of a spectrum of pure colors is shown. The image is constructed from the display of the red, green, and blue components at each wavelength shown in (b). (b) Red, green, and blue lines show the sRGB response function of the visible spectrum, as perceived by human vision. These three functions are multiplied by scattering spectra and summed individually to find the red, green, and blue components of the scattered light.

2. Reference Data

2.1 Reaction 2 for extended potential range

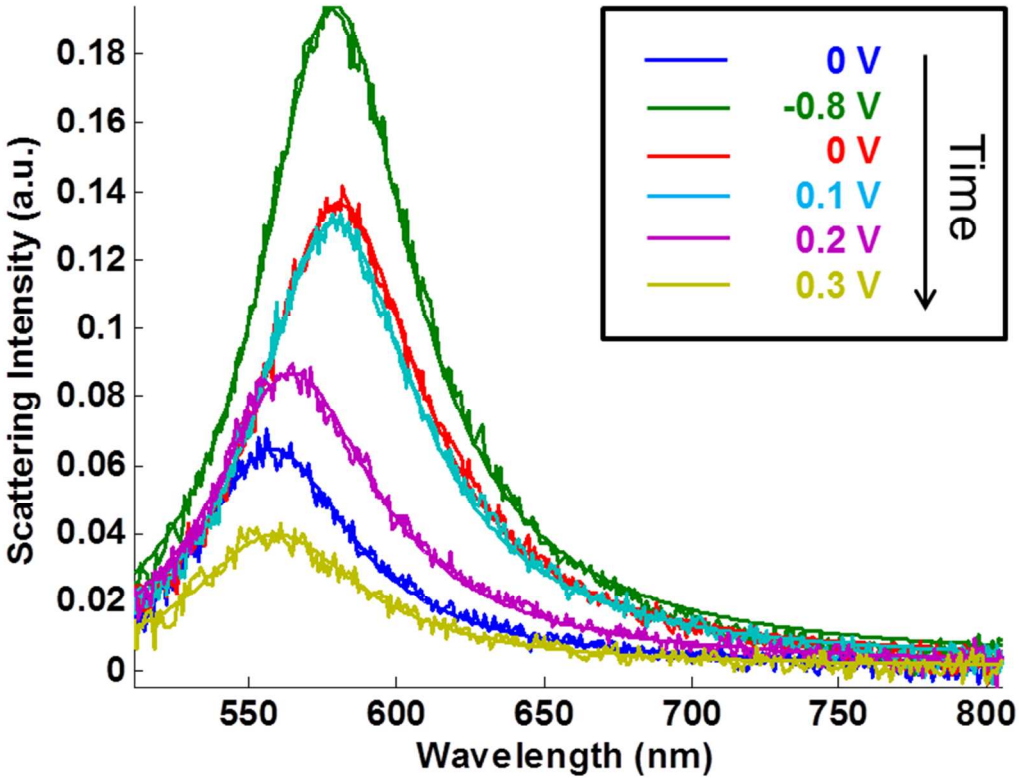

Figure S4. Nanoparticles characterized under Reaction 2 in Figure 2 of the main text return to their initial peak resonance energy only after a sufficient positive potential is applied. Steady-state scattering spectra from an example nanoparticle are shown above at given potentials. After a full potential cycle (blue, green, red), the plasmon resonance is still significantly red shifted and more intense. After the application of 100 mV (cyan), 200 mV (purple), and 300 mV (gold), the peak resonance has blue shifted back to approximately the same initial position. It is clear that the scattering intensity has decreased during this process, but this may be a result of minor focus drift during this longer experiment.

2.2 Scan rate dependence in the cathodic potential range

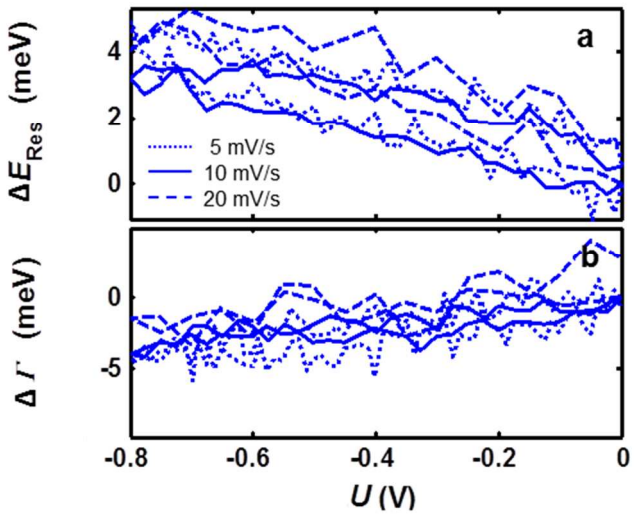

Figure S5. Comparison of the spectral response to varying scan rates in the cathodic range. (a) Change in peak resonance energy as a function of applied potential for three scan rates. There are small variations in the peak energy shift vs. potential slope but no systematic trend is observed. (b) The changes in plasmon resonance width as a function of applied potential for the three scan rates are nearly identical.

2.3 Sodium phosphate control experiment

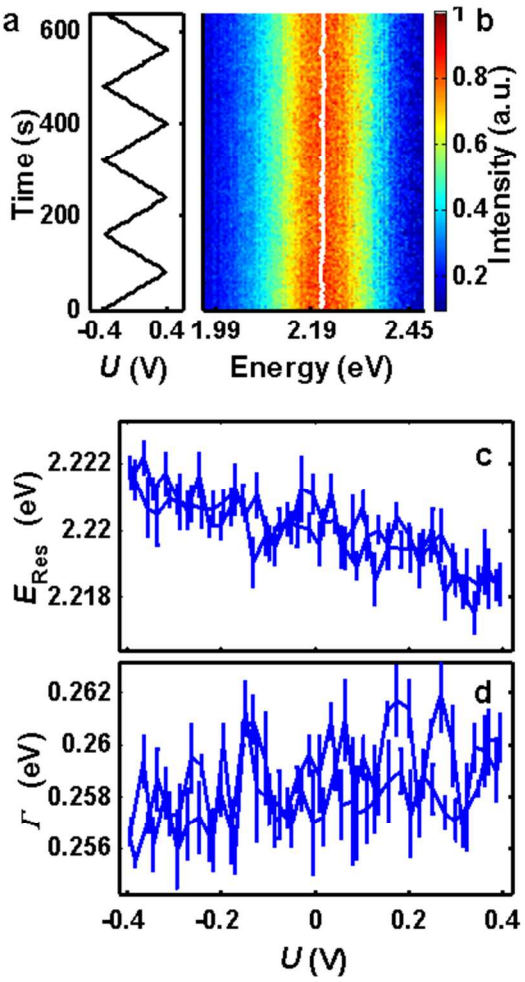

Figure S6. Linear surface plasmon resonance tuning of a 50 nm Au nanoparticle to potential modulation with an inert electrolyte in a combined cathodic and anodic potential range (-400 to +400 mV). (a) Electrochemical potential of the working electrode relative to the reference electrode as a function of time. Sweep rate: 10 mV/s. (b) Scattering spectra under dynamic potential control. (c) Reversible, linear E_{Res} response as a function of potential U shown as mean with standard error for five consecutive cycles. (d) Average Γ over five cycles as a function of potential. Electrolyte: 44 mM Na_2HPO_4. All potentials relative to silver/silver chloride quasi-reference electrode.

3. Charge density dependent scattering simulations

Charge density-modified Drude dielectric function for Mie scattering simulations

The following model was used to calculate the scattering efficiency of a plasmonically active metal nanosphere as a function of charge density. Following the general framework used in multiple works,[2-7] the effect of changes in the charge density of a nanoparticle can be modeled through the frequency dependent Drude dielectric function.

$$\varepsilon(\omega) = \varepsilon_{\infty} + \varepsilon_{free}$$

The free electron term depends on the free charge density via the bulk plasma frequency:

$$\varepsilon_{free}(\omega) = -\frac{\omega_p^2}{\omega^2 + i\gamma\omega}$$

where ω is the incident photon frequency, ω_p is the bulk plasma frequency, and γ is the damping coefficient. The bulk plasma frequency is given by:

$$\omega_p = \sqrt{\frac{Ne^2}{m\varepsilon_0}}$$

where N is the free charge density of the nanoparticle, e is the elementary charge, m is the effective mass of the electrons in the metal, and ε_0 is the free space permittivity. Through this simple model, the complex dielectric function of the metal as a function of free charge density can be found. The dielectric function of the metal can then be used to calculate the interaction of light with a nanoparticle of certain charge density using Mie Theory. In this study, the complex dielectric function of gold was calculated by subtracting the free electron term for an electrically neutral nanoparticle from smoothed Johnson and Christy tabulated optical data,[8] then adding the free electron term for the same nanoparticle with an altered free charge density. This scheme is represented in the following equation:

$$\varepsilon(\omega) = \varepsilon_{JC} - \varepsilon_{free}(neutral) + \varepsilon_{free}(charged)$$

The nanoparticle of interest was assumed to be 50 nm in diameter.. Gold nanoparticles in this study were supported on ITO (n = 1.922 at 550 nm) and immersed in 100 mM NaCl (n = 1.334 at 550 nm). In order to perform Mie theory calculations, the medium refractive index was treated as an adjustable parameter to fit the spectrum of the nanoparticle at open circuit potential. This procedure resulted in an effective refractive index of 1.4803, a reasonable value based on the refractive indices of the electrolyte solution and substrate. The refractive index value was then fixed and the charge density of the gold nanoparticle became the only fit parameter in the simulation. Figure S7 shows the large scale effect of changing the charge density of the nanoparticle. Here, simulated scattering spectra are shown for large changes to the free charge density. We found that changes in charge density were less than 1%. Mie theory simulations were performed in custom MATLAB scripts using 50 multipoles in the spherical harmonics expansion. Within the Drude model, the damping coefficient γ was fixed at 0.07 s^{-1}.

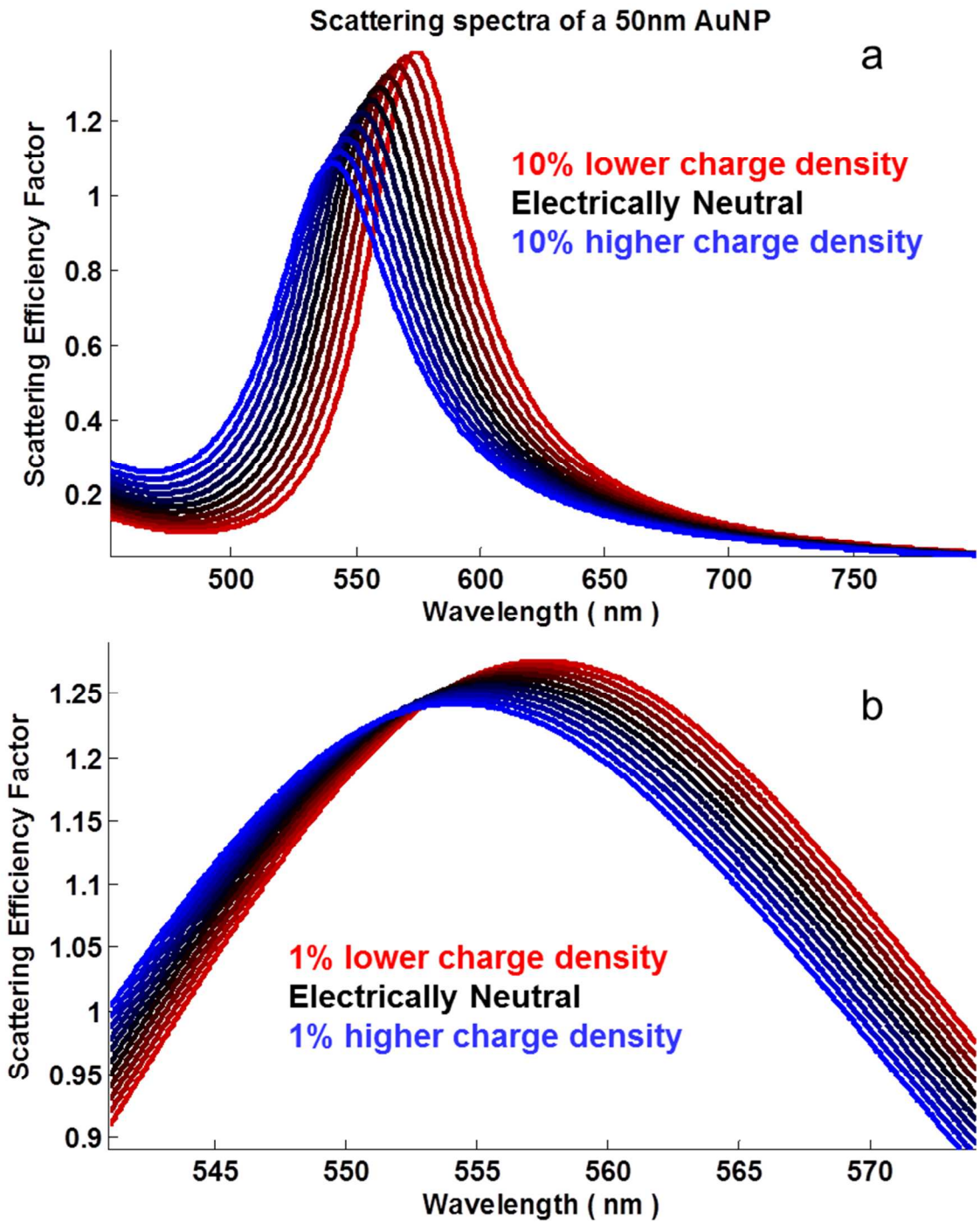

Figure S7. Calculated scattering spectra showing the effect of changing charge density of a gold nanosphere. A charge density-modified Drude dielectric function was used in Mie scattering calculations, which show that for increases in free charge density the resonance peak blue-shifts. (a) Full scattering spectra are shown for ±10% changes in the free charge density. Because the changes in charging were less than 1% of the total free electrons in a neutral nanoparticle during the experiment, a higher resolution excerpt is shown in (b). (b) The simulated scattering spectra for ±1% change in free

electron density. Note that the x-scale is in units of wavelength and not energy and that (b) shows a much smaller wavelength range than (a).

Because the charge density changes observed experimentally were so small, the simulated trends of the plasmon resonance on changes in charge density are shown in Figure S8 for a 50 nm gold nanoparticle. The resonance peak, the full width at half maximum, and the intensity are shown as a function of the fractional charge density. The fractional charge density is defined here as the free charge density of the nanoparticle divided by the free charge density of the same nanoparticle with no net electrical charge, that is, the number of free electrons in the neutral nanoparticle is equal to the number of gold atoms in the nanoparticle.

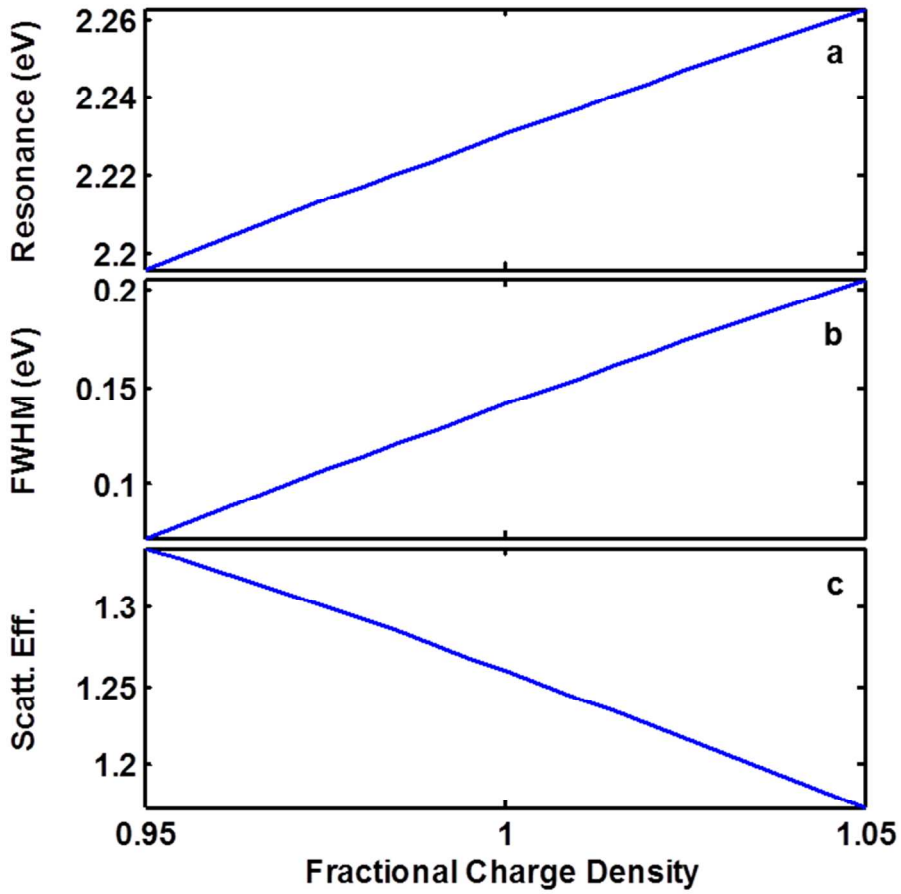

Figure S8. Charge density-modified Mie scattering calculations of resonance energy, full width at half maximum (FWHM), and scattering efficiency. The energy dependent dielectric function is calculated from smoothed Johnson and Christy data and modified by subtracting a Drude term calculated for an uncharged nanoparticle. The Drude term is then recalculated with a modified charge density and combined with the interband component. (a) Nanoparticle plasmon resonance as a function of the fractional charge density, according to the Mie-Drude model calculations. (b) The calculated FWHM shows that the trend in the resonance width is the opposite of what is seen in experiment. The FWHM is expected to increase at cathodic potentials but instead it decreases. Likewise, at anodic potentials where the free electron density decreases, the FWHM is predicted to decrease but actually increases for all observed nanoparticles. (c) Similarly, the model predicts that for higher charge densities, the scattering efficiency factor should slightly decrease, but the opposite is observed in experiments. We interpret this as an indication that a mechanism other than the charge density of the nanoparticle is responsible for changes in resonance width and scattering intensity.

4. Indium Tin Oxide carrier concentration tuning simulations

Because the particles are not an isolated system, the effect of changing the carrier mobility of the indium tin oxide thin film was modeled using a Drude Lorentz function to calculate the refractive index as a function of carrier density. Literature values were used for the uncharged free carrier density, and carrier scattering time (5×10^{20} carriers/cm^3, 4 fs).[9-10] The Drude-Lorenz model results matched literature results and experimental measurements.[9]

Mie scattering calculations were then performed for a 50 nm Au sphere embedded in this tunable ITO medium. The free electron density of the gold was fixed in order to assess the role of ITO carrier density tuning only. It is important to note that in this model, the nanoparticle is embedded in the medium, and this can be interpreted as an upper limit for plasmon resonance modulation. In our experimental configuration, ITO only forms the substrate and therefore constitutes a very small fraction of the nanoparticle surface area contact with its embedding medium.

Over a very large carrier density tuning range (>1 order of magnitude carriers/cm^3) a nearly linear dependence can be seen for resonance energy, width, and scattering efficiency. The observed trends qualitatively match the experimental trend for resonance energy but are opposite of those observed for FWHM and scattering efficiency. According to Dasgupta et al.[11] the charge carrier density of ITO thin films under electrochemical gating only changed at a rate of 1.7 x 10^{13} electrons/cm^3 per volt. While this 0.0000034 % change in carrier density per volt was electrically measureable for Dasgupta et al., the corresponding change in the refractive index is $\Delta n = 4 \times 10^{-9}$ Mie scattering simulations were performed using a 50 multipole expansion and a carrier concentration tuned refractive index over a range of 4 x 10^{20} to 6×10^{20} carriers/cm^3. All

scattering parameters as a function of carrier concentration were fit well with a linear regression. The fit parameters are summarized in Table S1 along with the calculated shift in each parameter using the measured carrier density variation reported by Dasgupta et al. As can be seen in column four of Table S1, all changes are several orders of magnitude lower than any experimental noise level and would therefore not be measureable. In order to produce the measured 4 meV shift shown in Figure 3 of the manuscript, the carrier concentration would need to change by 3.4×10^{19} carriers/cm^3. This concentration change is roughly 6 million times larger than that measured by Dasgupta et al. over a similar potential range. Because this embedded nanoparticle model is viewed as the upper limit for the ITO carrier concentration tuning effect, we conclude that this mechanism is not a contributor to the observed electrochemical plasmon tuning.

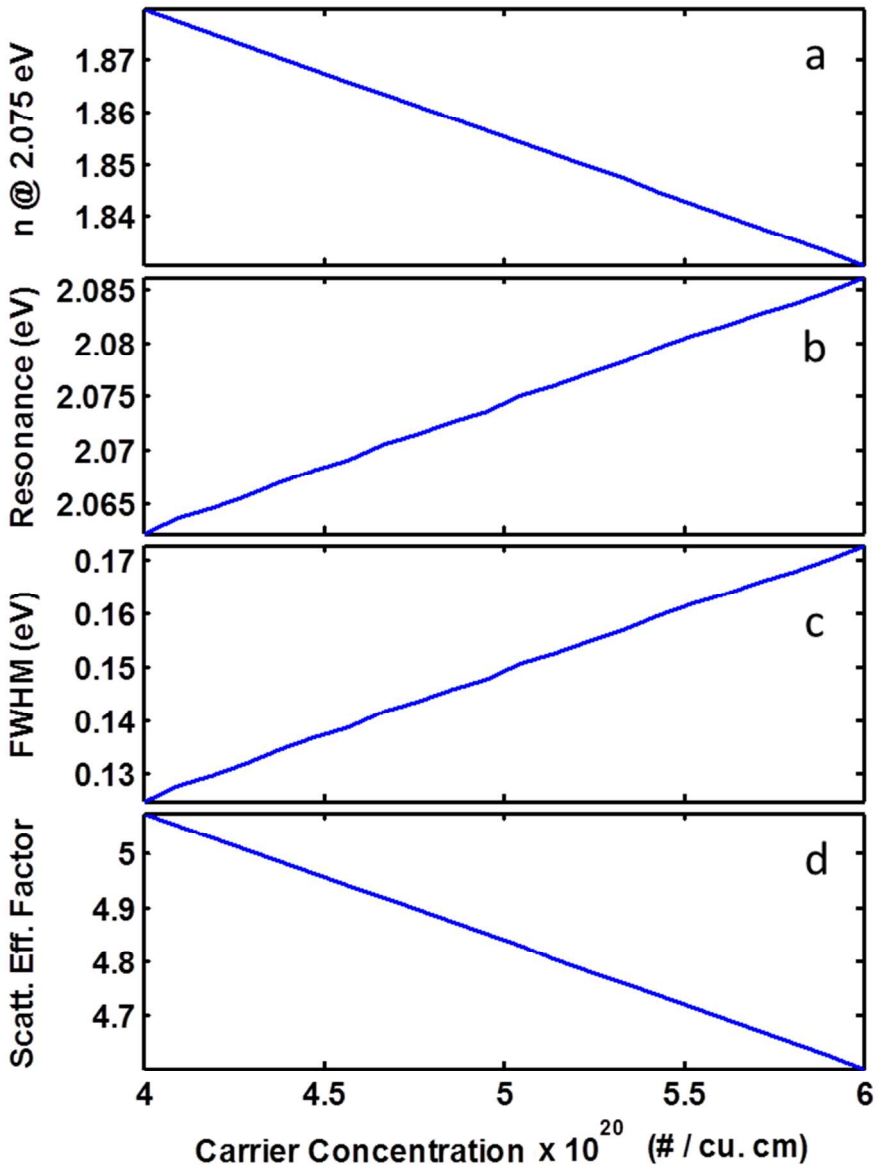

Figure S9. Mie Scattering simulations of the plasmon resonance scattering of a 50 nm Au sphere embedded in a charge carrier tunable Indium Tin Oxide (ITO) thin film. The refractive index at 2.075 eV (a), resonance energy (b), resonance width (c), and scattering efficiency factor (d) are shown as a function of the charge carrier concentration of ITO around a literature-reported charge-neutral range. Each trend was fit with a linear regression. Fit parameters are shown in Table S1, along with predicted changes for literature-reported changes in ITO charge carrier concentration.

Model: Y = mx+b	**m**	**b**	**Calculated change using x=ΔN = 1.7 x 10^{13}**
Refractive Index, n @ 2.075 eV	-2.47 x 10^{-22}	1.98	4.20 x 10^{-9}
Resonance energy, E_{Res}	1.19 x 10^{-22}	2.02	2.02 x 10^{-9} eV
Full Width at Half Maximum, Γ	2.37 x 10^{-22}	0.0305	4.04 x 10^{-9} eV
Scattering Efficiency Factor	-2.37 x 10^{-21}	6.03	-4.03 x 10^{-8}

Table S1. Linear regression fit parameters for the trends in Figure S9 are reported along with predicted values for 1 V change in electrochemical potential using literature reported changes in carrier concentration. Even for an entirely embedded nanoparticle, the resonance energy, resonance width, and scattering intensity changes would be roughly six orders of magnitude too small to experimentally probe directly with our method.

References

1. Gupta, R.; Hartley, R. I., Linear pushbroom cameras. *IEEE T. Pattern. Anal.* **1997,** *19*, 963-975.
2. Mulvaney, P.; Perez-Juste, J.; Giersig, M.; Liz-Marzan, L. M.; Pecharroman, C., Drastic surface plasmon mode shifts in gold nanorods due to electron charging. *Plasmonics* **2006,** *1*, 61-66.
3. Ung, T.; Giersig, M.; Dunstan, D.; Mulvaney, P., Spectroelectrochemistry of Colloidal Silver. *Langmuir* **1997,** *13*, 1773-1782.
4. Novo, C.; Funston, A. M.; Mulvaney, P., Direct observation of chemical reactions on single gold nanocrystals using surface plasmon spectroscopy. *Nat. Nano.* **2008,** *3*, 598-602.
5. Novo, C.; Funston, A. M.; Gooding, A. K.; Mulvaney, P., Electrochemical charging of single gold nanorods. *J. Am. Chem. Soc.* **2009,** *131*, 14664-6.
6. Mulvaney, P., Surface Plasmon Spectroscopy of Nanosized Metal Particles. *Langmuir* **1996,** *12*, 788-800.
7. Chapman, R.; Mulvaney, P., Electro-optical shifts in silver nanoparticle films. *Chem. Phys. Lett.* **2001,** *349*, 358-362.
8. Johnson, P. B.; Christy, R. W., Optical Constants of the Noble Metals. *Phys. Rev. B* **1972,** *6*, 4370-4379.
9. Sorger Volker, J.; Lanzillotti-Kimura Norberto, D.; Ma, R.-M.; Zhang, X., Ultra-compact silicon nanophotonic modulator with broadband response. In *Nanophotonics*, 2012; Vol. 1, p 17.
10. Brewer, S. H.; Franzen, S., Calculation of the electronic and optical properties of indium tin oxide by density functional theory. *Chem. Phys.* **2004,** *300*, 285-293.
11. Dasgupta, S.; Lukas, M.; Dössel, K.; Kruk, R.; Hahn, H., Electron mobility variations in surface-charged indium tin oxide thin films. *Phys. Rev. B* **2009,** *80*, 085425.